AIAA AVIATION Forum
13-17 June 2016, Washington, D.C.
34th AIAA Applied Aerodynamics Conference

Delayed Detached Eddy Simulation of Supersonic Panel Aeroelasticity Using Fully Coupled Fluid Structure Interaction with High Order Schemes

Jiaye Gan*, Gecheng Zha†
Dept. of Mechanical and Aerospace Engineering
University of Miami
Coral Gables, FL 33124
gzha@miami.edu

Abstract

This paper conducts delayed detached eddy simulation of a supersonic panel vibration at Mach 2.0. Unsteady 3D compressible Navier-Stokes equations are solved with a system of 5 decoupled structure modal equations in a fully coupled manner. The low diffusion E-CUSP scheme with a 5th order WENO reconstruction for the inviscid flux and a set of 2nd order central differencing for the viscous terms are used to accurately capture the shock wave/turbulent boundary layer interaction of the vibrating panel. The shock waves and their reflection interacting with turbulent boundary layer in the tunnel are well captured by the DDES. The panel vibration induced by the shock boundary layer interaction is well resolved by the simulation. The panel response agrees well with the experiment in terms of the mean panel displacement and frequency. Since it is a fully coupled fluid-structural interaction simulation, the flow and structure responses are captured by the solver itself with no parameter adjustment. The simulation is fairly efficient due to the high order schemes. It takes one week wall clock time to run 0.1s physical time with 264 CPUs using parallel computing.

1 Introduction

Supersonic panel flutter is a self-excited aeroelastic instability which typically has high amplitude and may cause fatigue damage. Study of supersonic panel flutter is very important for supersonic/hypersonic vehicle design. However, high fidelity numerical simulation of supersonic panel flutter is very challenging due to the complex shock-turbulent boundary layer interaction(STBLI). For the structure, the skin panel temperature could be sufficiently high to cause large nonlinear deflection.

Many previous research efforts on the prediction of panel flutter are based on analytical and experimental methods. The analytical methods include the governing partial differential equations (PDE) in conjunction with the Galerkin method[1] and the finite element methods[2] for nonlinear supersonic panel flutter. The aerodynamic models used in those methods are mainly linearized, such as linear piston and linearized potential flow model. However, linear aerodynamic models are difficult to resolve STBLI since the flows are inherently non-linear and unsteady. STBLI may result in an amplification of heating, aeroacoustic loading, and flow separation. Priebe et al[3] employed direct numerical simulation (DNS) to study the STBLI on a ramp configuration. They demonstrate that the shock impingement amplifies the pressure fluctuation and there are high-level, low-frequency (< 1000 Hz) vortex structures in the turbulent boundary layer. Although numerical simulations using Reynolds Averaged Navier

* Ph.D. Candidate
† Ph.D., Professor, Director of Aerodynamics and CFD Lab

Stokes (RANS)[4, 5], large eddy simulation (LES)[6], and direct numerical simulation (DNS)[4, 3] have been utilized to study the STBLI, few work is focused specifically on the analysis of STBLIs on panel aeroelasticity.

To consider the viscous effect of transonic flutter prediction, RANS models are often used as a more affordable way than LES. However, RANS models in general can not accurately resolve the flow separation caused by shock boundary layer interaction since RANS models are based on non-physical assumption that large vortex structures are isotropic. Morgan et al.[6] introduce shock unsteadiness correction to improve RANS model's accuracy on shock boundary layer interaction. Large Eddy Simulation(LES) is more plausible than RANS models since LES directly simulates the large eddy structures and models the small eddies, which is more isotropic. However, LES could be preventive CPU expensive for the high Reynolds number hypersonic flows due to the excessive mesh size required.

The hybrid RANS/LES approach, Detached eddy simulation (DES) suggested by Spalart[7], is developed for complex turbulence problems as a compromise between prediction accuracy and CPU efficiency. In DES, a RANS model is used within wall boundary layers to reduce the grid density, and LES is used outside the wall boundary layer to deal with massively separated flows. Spalart et al[7] suggested delayed DES(DDES) in 2006 to overcome the modeled stress depletion(MSD) problem of the original DES when the mesh is thin compared with boundary layer thickness. In DDES, a blending function similar to the one used by Mentor and Kuntz[8] for the SST model is introduced to limit the length scale of DES97 to ensure the transition of RANS to LES to be independent of grid spacing.

Crowell et al[9] developed a CFD-FEM based partitioned aerothermal solver to investigate the thermal response of surface panels subject to shock turbulent boundary layer interaction. Their results show that a static approximation, in which the flow is simulated a priori without consideration of the surface motion, significantly under predicts the peak temperature rise and affects the length deformation of the panel. Dechaumphai et al[10] used 2D finite element fluid-thermal-structural solver to study hypersonic flow over metallic thin panels in both aligned and inclined configurations with respect to the free stream. Their results show that even very modest deformations alter flow features including shocks, expansions, and separation that significantly influence the heat load. Also, their CFD-FEM solver is only implemented for two dimensional problems in loosely coupled manner. Gogulapati et al[11] studied the flow-structural response of thin-gauge panels subject to shock impingement with steady CFD and reduced order of FEM method. The unsteady pressure fluctuation on the panel surface is estimated by the surrogate of the steady CFD and empirical correlation. The computed dynamic panel displacements are largely deviated from experiment up to a few orders of magnitude.

The loosely coupled fluid-structural interaction(FSI) methods, in which the structural response lags behind the flow field solution, are widely used for their simplicity of coding and CPU efficiency. This type of methods may be limited to first-order accuracy regardless of the accuracy of the individual flow and structure solvers[12]. In the fully coupled FSI methods, the flow field and structure always respond simultaneously by exchanging the aerodynamic forcing and structural displacement within each iteration. Strictly speaking, only the fully coupled methods are rigorous in the physical sense because, in reality, the structural displacement responds simultaneously with the forces acted by the fluid. Among the researchers in the area of 3-D time-marching aeroelastic analysis based on Euler/Navier Stokes approaches, Lee-Rausch and Batina[13] used a three factor, implicit, upwind-biased Euler/Navier Stokes approach loosely coupled with a lagged structure solver. Morton, Melville and Gordnier et al.[14, 15, 16] developed an implicit fully coupled fluid-structure interaction model, which used the Beam-Warming implicit approximate factorization scheme for the flow solver coupled with a modal structural solver. Liu et al[17]. developed a fully coupled method using Jameson's explicit scheme with a multigrid approach utilizing the Euler equations and a modal structural model.

The other very important issue of FSI simulation is the artificial dissipation from the CFD schemes, which affects the prediction of aerodynamic damping to the structure. It includes the resolution of acoustic waves and high order mode of panel vibration with high reduced frequency, which is a small

scale wave phenomenon. Most of the current CFD simulations for FSI use 2nd or 3rd order schemes for the convective fluxes, which have high numerical dissipation due to the upwinding requirement to capture shock waves. The authors' group has developed high order shock capturing schemes for FSI with 5th order weighted essentially non-oscillatory (WENO) scheme for inviscid fluxes[18, 19, 20, 21, 22].

The advantage of high order low diffusion schemes is shown in the simulation of the transonic NLR 7301 airfoil limited cycle oscillation (LCO). Since the LCO has bifurcation, some simulations using 2nd order schemes are only able to capture the amplitude about 10 times higher than the measured one in wind tunnel. Their schemes tend to be too diffusive to capture the LCO with the amplitude as small as 2/1000 of the airfoil chord. The simulation of Wang et al.[20, 21] of the present author's group is the only one, and the first one, that accurately captures the small LCO amplitude measured in the experiment.

Chen et al.[23] have developed a fully coupled methodology between fluid and structure for predicting 3-D transonic wing flutter. In the fully coupled FSI[23], the governing equations of structural and fluid motion are simultaneously solved by exchanging the unsteady aerodynamic force and structural displacement within each physical time step via a successive iteration on the pseudo-time step. In[23], the computed flutter boundary of AGARD wing 445.6 at free stream Mach numbers ranging from 0.499 to 1.141 agrees well with the experiment. In the work of Im et al.[24], a fully coupled FSI developed by Chen et al.[23] is extended to turbomachinery by implementing an advanced blade tip deforming mesh technique to capture the transonic rotor flutter. The fully coupled FSI methodology is adopted in this study. The methodology and code are shown to accurately predict the flutter boundary of a transonic single rotor[24] and AGARD wing with the shock/boundary layer interaction[25, 26].

The purpose of this paper is to simulate supersonic fluid-structural interaction of a flat panel using Delayed Detached Eddy Simulation with high order shock capturing scheme. As the first step, the motion of the panel is treated using linear modal approach. The dynamic motion of the panel is decoupled with the first 5 modes and is solved with Navier-Stokes equations in a fully coupled manner as described in[23]. The in house code FASIP(Flow-Acoustic-Structure Interaction Package) with high order schemes and fully coupled FSI[27] is employed.

2 Numerical Algorithm

2.1 Governing Equations

The governing equations for the flow field computation are the spatially filtered 3D time accurate compressible Navier-Stokes equations in generalized coordinates(ξ, η, ζ) and can be expressed as the following conservative form:

$$\frac{\partial \mathbf{Q}}{\partial t} + \frac{\partial \mathbf{E}}{\partial \xi} + \frac{\partial \mathbf{F}}{\partial \eta} + \frac{\partial \mathbf{G}}{\partial \zeta} = \frac{1}{Re}\left(\frac{\partial \mathbf{E}_v}{\partial \xi} + \frac{\partial \mathbf{F}_v}{\partial \eta} + \frac{\partial \mathbf{G}_v}{\partial \zeta}\right) + \mathbf{S} \tag{1}$$

where Re is the Reynolds number. Delayed detached eddy simulation(DDES) turbulence model introduced by Sparlat et al.[7] is used to close the system of equations. The equations are nondimenisonalized based on the blade chord length L_∞, upstream characteristic density ρ_∞ and velocity U_∞.

The conservative variable vector $\mathbf{Q}$, the inviscid flux vectors $\mathbf{E}$, $\mathbf{F}$, $\mathbf{G}$, the viscous fluxs $\mathbf{E_v}$, $\mathbf{F_v}$, $\mathbf{G_v}$ and the source term vector $\mathbf{S}$ are expressed as

$$\mathbf{Q} = \frac{1}{J}\begin{pmatrix} \bar{\rho} \\ \bar{\rho}\tilde{u} \\ \bar{\rho}\tilde{v} \\ \bar{\rho}\tilde{w} \\ \bar{\rho}\tilde{e} \\ \bar{\rho}\tilde{\nu} \end{pmatrix}, \mathbf{E} = \begin{pmatrix} \bar{\rho}U \\ \bar{\rho}\tilde{u}U + l_x\bar{p} \\ \bar{\rho}\tilde{v}U + l_y\bar{p} \\ \bar{\rho}\tilde{w}U + l_z\bar{p} \\ \left(\bar{\rho}\tilde{e} + \bar{p}\right)U - l_t\bar{p} \\ \bar{\rho}\tilde{\nu}U \end{pmatrix} \tag{2}$$

$$\mathbf{F} = \begin{pmatrix} \bar{\rho}V \\ \bar{\rho}\tilde{u}V + m_x\bar{p} \\ \bar{\rho}\tilde{v}V + m_y\bar{p} \\ \bar{\rho}\tilde{w}V + m_z\bar{p} \\ \left(\bar{\rho}\tilde{e} + \bar{p}\right)V - m_t\bar{p} \\ \bar{\rho}\tilde{\nu}V \end{pmatrix} \tag{3}$$

$$\mathbf{G} = \begin{pmatrix} \bar{\rho}W \\ \bar{\rho}\tilde{u}W + n_x\bar{p} \\ \bar{\rho}\tilde{v}W + n_y\bar{p} \\ \bar{\rho}\tilde{w}W + n_z\bar{p} \\ \left(\bar{\rho}\tilde{e} + \bar{p}\right)W - n_t\bar{p} \\ \bar{\rho}\tilde{\nu}W \end{pmatrix} \tag{4}$$

$$\mathbf{E_v} = \begin{pmatrix} 0 \\ l_k\bar{\tau}_{xk} \\ l_k\bar{\tau}_{yk} \\ l_k\bar{\tau}_{zk} \\ l_k\left(\tilde{u}_i\bar{\tau}_{ki} - \bar{q}_k\right) \\ \frac{\bar{\rho}}{\sigma}\left(\nu + \tilde{\nu}\right)\left(\mathbf{l} \bullet \nabla\tilde{\nu}\right) \end{pmatrix} \tag{5}$$

$$\mathbf{F_v} = \begin{pmatrix} 0 \\ m_k\bar{\tau}u_{xk} \\ m_k\bar{\tau}_{yk} \\ m_k\bar{\tau}u_{zk} \\ m_k\left(\tilde{u}_i\bar{\tau}_{ki} - \bar{q}_k\right) \\ \frac{\bar{\rho}}{\sigma}\left(\nu + \tilde{\nu}\right)\left(\mathbf{m} \bullet \nabla\tilde{\nu}\right) \end{pmatrix} \tag{6}$$

$$\mathbf{G_v} = \begin{pmatrix} 0 \\ n_k\bar{\tau}_{xk} \\ n_k\bar{\tau}_{yk} \\ n_k\bar{\tau}_{zk} \\ n_k\left(\tilde{u}_i\bar{\tau}_{ki} - \bar{q}_k\right) \\ \frac{\bar{\rho}}{\sigma}\left(\nu + \tilde{\nu}\right)\left(\mathbf{n} \bullet \nabla\tilde{\nu}\right) \end{pmatrix} \tag{7}$$

$$\mathbf{S} = \frac{1}{J}\begin{pmatrix} 0 \\ 0 \\ 0 \\ 0 \\ 0 \\ S_\nu \end{pmatrix} \tag{8}$$

where ρ is the density, p is the static pressure, and e is the total energy per unit mass. The overbar denotes a regular filtered variable, and the tilde is used to denote the Favre filtered variable. U, V and W are the contravariant velocities in ξ, η, ζ directions, and defined as follows.

$$U = l_t + \mathbf{l} \bullet \mathbf{V} = l_t + l_x\tilde{u} + l_y\tilde{v} + l_z\tilde{w} \tag{9}$$

$$V = m_t + \mathbf{m} \bullet \mathbf{V} = m_t + m_x\tilde{u} + m_y\tilde{v} + m_z\tilde{w} \tag{10}$$

$$W = n_t + \mathbf{n} \bullet \mathbf{V} = n_t + n_x\tilde{u} + n_y\tilde{v} + n_z\tilde{w} \tag{11}$$

where l_t, m_t and n_t are the components of the interface contravariant velocity of the control volume in ξ, η and ζ directions respectively. $\mathbf{l}$, $\mathbf{m}$ and $\mathbf{n}$ denote the normal vectors located at the centers of ξ, η and ζ interfaces of the control volume with their magnitudes equal to the surface areas and pointing to the directions of increasing ξ, η and ζ. J is the Jacobian of the transformation. The source term S_ν in eq. (8), is given by

$$\begin{array}{c} S_\nu = \bar{\rho}C_{b1}\left(1 - f_{t2}\right)\tilde{S}\tilde{\nu} \\ +\frac{1}{Re}\left[-\bar{\rho}\left(C_{w1}f_w - \frac{C_{b1}}{\kappa^2}f_{t2}\right)\left(\frac{\tilde{\nu}}{d}\right)^2\right. \\ \left.+\frac{\bar{\rho}}{\sigma}C_{b2}\left(\nabla\tilde{\nu}\right)^2 - \frac{1}{\sigma}\left(\tilde{\nu} + \tilde{\nu}\right)\nabla\tilde{\nu} \bullet \nabla\bar{\rho}\right] \\ +Re\left[\bar{\rho}f_{t1}\left(\Delta q\right)^2\right] \end{array} \tag{12}$$

where

$$\tilde{\nu} = \nu f_{v1} \qquad \chi = \frac{\tilde{\nu}}{\nu} \tag{13}$$

$$f_{v1} = \frac{\chi^3}{\chi^3 + c_{v1}^3} \qquad f_{v2} = 1 - \frac{\chi}{1 + \chi f_{v1}} \tag{14}$$

$$f_{t1} = C_{t1}g_t exp\left[-C_{t2}\frac{\omega_t^2}{\Delta U^2}\left(d^2 + g_t^2 d_t^2\right)\right] \tag{15}$$

$$f_{t2} = C_{t3}exp\left(-C_{t4}\chi^2\right) \qquad f_w = g(\frac{1 + c_{w3}^6}{g^6 + c_{w3}^6})^{1/6} \tag{16}$$

$$g = r + c_{w2}(r^6 - r) \qquad g_t = min\left(0.1, \frac{\Delta q}{\omega_t \Delta x_t}\right) \tag{17}$$

$$\tilde{S} = S + \frac{\tilde{\nu}}{k^2 d^2} f_{v2} \tag{18}$$

$$r = \frac{\tilde{\nu}}{\tilde{S}k^2 d^2} \tag{19}$$

where, ω_t is the wall vorticity at the wall boundary layer trip location, d is the distance to the closest wall, d_t is the distance of the field point to the trip location, Δq is the difference of the velocities between the field point and the trip location, Δx_t is the grid spacing along the wall at the trip location. The values of the coefficients are: $c_{b1} = 0.1355, c_{b2} = 0.622, \sigma = \frac{2}{3}, c_{w1} = \frac{c_{b1}}{k^2} + (1 + c_{b2})/\sigma, c_{w2} = 0.3, c_{w3} = 2, k = 0.41, c_{v1} = 7.1, c_{t1} = 1.0, c_{t2} = 2.0, c_{t3} = 1.1, c_{t4} = 2.0$.

The shear stress $\bar{\tau}_{ik}$ and total heat flux $\bar{q}_k$ in Cartesian coordinates is given by

$$\bar{\tau}_{ik} = \left(\tilde{\mu} + \tilde{\mu}_{DES}\right)\left[\left(\frac{\partial\tilde{u}_i}{\partial x_k} + \frac{\partial\tilde{u}_k}{\partial x_i}\right) - \frac{2}{3}\delta_{ik}\frac{\partial\tilde{u}_j}{\partial x_j}\right] \tag{20}$$

$$\bar{q}_k = -\left(\frac{\tilde{\mu}}{Pr} + \frac{\tilde{\mu}_{DES}}{Pr_t}\right)\frac{\partial\tilde{T}}{\partial x_k} \tag{21}$$

where μ is from Sutherland's law, and $\mu_{DES}(=\bar{\rho}\tilde{\nu}f_{v1})$ is determined by DES model. The above equations are in tensor form, where the subscripts i,k represents the coordinates x,y,z and the Einstein summation convention is used. Eq.(20) and (21) are transformed to the generalized coordinate system in computation.

In DES, a modification of a S-A based RANS model in which the model switches to a subgrid scale formulation in regions for LES calculations. The coefficients c_{t1} and c_{t3} in the S-A model are set to zero and the distance to the nearest wall, d, is replaced by $\tilde{d}$ as

$$\tilde{d} = min(d, C_{DES}\Delta) \tag{22}$$

where Δ is the largest spacing of the grid cell in all the directions. Within the boundary layer close to the wall, $\tilde{d} = d$, hence the turbulence is simulated by RANS mode of Spalart-Allmaras[28]. Away from the boundary layer, $\tilde{d} = C_{DES}\Delta$ is most of the cases. When the production and destruction terms of the model are balanced, the length scale $\tilde{d}$ will have a Smagorinsky-like eddy viscosity and the turbulence is simulated by the LES model. The coefficient $C_{DES} = 0.65$ is used as set in the homogeneous turbulence[29]. The Pr_t may take the value of 0.9 within the boundary layer for RANS mode and 0.5 for LES mode away from the wall surface.

To overcome the modeled stress depletion problem and make the DES limiter independent of grid spacing, the DDES model suggested by Spalart et al.[7] switches the subgrid scale formulation in DES model by redefining the distance to the nearest wall $\tilde{d}$ as

$$\tilde{d} = d - f_d max(0, d - C_{DES}\Delta) \tag{23}$$

where

$$f_d = 1 - tanh([8r_d]^3) \tag{24}$$

$$r_d = \frac{\nu_t + \nu}{(U_{i,j}U_{i,j})^{0.5}k^2d^2R_e} \tag{25}$$

$$U_{i,j} = \frac{\partial u_i}{\partial x_j} \tag{26}$$

$U_{i,j}$ represents the velocity gradient, and k denotes the Karmann constant. Within the boundary layer close to walls, $\tilde{d} = d$, and away from the boundary layer, $\tilde{d} = d - f_d(d - C_{DES}\Delta)$ is most of the case. This mechanism enables DDES to behave as a RANS model in the near-wall region, and LES away from walls. This modification in $\tilde{d}$ reduces the grey transition area between RANS and LES.

The equation of state as a constitutive equation relating density to pressure and temperature is defined as:

$$\bar{\rho}\tilde{e} = \frac{\bar{p}}{(\gamma - 1)} + \frac{1}{2}\bar{\rho}(\tilde{u}^2 + \tilde{v}^2 + \tilde{w}^2) \tag{27}$$

where γ is the ratio of specific heats. For simplicity, all the bar and tilde in above equations will be dropped in the rest of this paper.

2.2 The Low Diffusion E-CUSP Scheme for Inviscid Flux

The Low Diffusion E-CUSP(LDE) Scheme[30, 31] is used to evaluate the inviscid fluxes. The basic idea of the LDE scheme is to split the inviscid flux into the convective flux E^c and the pressure flux E^p based on the upwind characteristics. With an extra equation from the DDES model, the splitting is basically the same as the original scheme for the Euler equation. This is an advantage over the Roe scheme[32], for which the eigenvectors need to be derived when any extra equation is added to the governing equations. In generalized coordinate system, the flux $\mathbf{E}$ can be split as the following:

$$\mathbf{E}' = E^c + E^p = \begin{pmatrix} \rho U \\ \rho u U \\ \rho v U \\ \rho w U \\ \rho e U \\ \rho \tilde{\nu} U \end{pmatrix} + \begin{pmatrix} 0 \\ l_x p \\ l_y p \\ l_z p \\ p\overline{U} \\ 0 \end{pmatrix} \tag{28}$$

where, U is the contravariant velocity in ξ direction and is defined as the following:

$$U = l_t + l_x u + l_y v + l_z w \tag{29}$$

$\overline{U}$ is defined as:

$$\overline{U} = l_x u + l_y v + l_z w \tag{30}$$

The convective term, E^c is evaluated by

$$E^c = \rho U \begin{pmatrix} 1 \\ u \\ v \\ w \\ e \\ \tilde{\nu} \end{pmatrix} = \rho U f^c,\ f^c = \begin{pmatrix} 1 \\ u \\ v \\ w \\ e \\ \tilde{\nu} \end{pmatrix} \tag{31}$$

let

$$C = c\left(l_x^2 + l_y^2 + l_z^2\right)^{\frac{1}{2}} \tag{32}$$

where $c = \sqrt{\gamma RT}$ is the speed of sound.

Then the convective flux at interface $i + \frac{1}{2}$ is evaluated as:

$$E^c_{i+\frac{1}{2}} = C_{\frac{1}{2}} \left[\rho_L C^+ f^c_L + \rho_R C^- f^c_R\right] \tag{33}$$

where, the subscripts L and R represent the left and right hand sides of the interface. The Mach number splitting of Edwards[33] is borrowed to determine c^+ and c^- as the following:

$$C_{\frac{1}{2}} = \frac{1}{2}\left(C_L + C_R\right) \tag{34}$$

$$C^+ = \alpha^+_L \left(1 + \beta_L\right) M_L - \beta_L M^+_L - M^+_{\frac{1}{2}} \tag{35}$$

$$C^- = \alpha^-_R \left(1 + \beta_R\right) M_R - \beta_R M^-_R + M^-_{\frac{1}{2}} \tag{36}$$

$$M_L = \frac{U_L}{C_{\frac{1}{2}}},\ M_R = \frac{U_R}{C_{\frac{1}{2}}} \tag{37}$$

$$\alpha_{L,R} = \frac{1}{2}\left[1 \pm sign\left(M_{L,R}\right)\right] \tag{38}$$

$$\beta_{L,R} = -max\left[0, 1 - int\left(|M_{L,R}|\right)\right] \tag{39}$$

$$M^{+}_{\frac{1}{2}} = M_{\frac{1}{2}}\frac{C_R + C_L\Phi}{C_R + C_L},\ M^{-}_{\frac{1}{2}} = M_{\frac{1}{2}}\frac{C_L + C_R\Phi^{-1}}{C_R + C_L} \tag{40}$$

$$\Phi = \frac{\left(\rho C^2\right)_R}{\left(\rho C^2\right)_L} \tag{41}$$

$$M_{\frac{1}{2}} = \beta_L\delta^{+}M^{-}_{L} - \beta_R\delta^{-}M^{+}_{R} \tag{42}$$

$$M^{\pm}_{L,R} = \pm\tfrac{1}{4}\left(M_{L,R} \pm 1\right)^2 \tag{43}$$

$$\delta^{\pm} = \tfrac{1}{2}\left\{1 \pm sign\left[\tfrac{1}{2}\left(M_L + M_R\right)\right]\right\} \tag{44}$$

The pressure flux, E^p is evaluated as the following

$$E^{p}_{i+\frac{1}{2}} = \begin{pmatrix} 0 \\ \mathcal{P}^{+}p\,l_x \\ \mathcal{P}^{+}p\,l_y \\ \mathcal{P}^{+}p\,l_z \\ \frac{1}{2}p\left[\overline{U} + \overline{C}_{\frac{1}{2}}\right] \\ 0 \end{pmatrix}_L + \begin{pmatrix} 0 \\ \mathcal{P}^{-}p\,l_x \\ \mathcal{P}^{-}p\,l_y \\ \mathcal{P}^{-}p\,l_z \\ \frac{1}{2}p\left[\overline{U} - \overline{C}_{\frac{1}{2}}\right] \\ 0 \end{pmatrix}_R \tag{45}$$

The contravariant speed of sound $\overline{C}$ in the pressure vector is consistent with $\overline{U}$. It is computed based on C as the following,

$$\overline{C} = C - l_t \tag{46}$$

The use of $\overline{U}$ and $\overline{C}$ instead of U and C in the pressure vector is to take into account of the grid speed so that the flux will transit from subsonic to supersonic smoothly. When the grid is stationary, $l_t = 0$, $\overline{C} = C$, $\overline{U} = U$.

The pressure splitting coefficient is:

$$\mathcal{P}^{\pm}_{L,R} = \frac{1}{4}\left(M_{L,R} \pm 1\right)^2\left(2 \mp M_L\right) \tag{47}$$

The LDE scheme can capture crisp shock profile and exact contact surface discontinuities as accurately as the Roe scheme[31]. However, it is simpler and more CPU efficient than the Roe scheme due to no matrix operation. In the reference[34], the LDE scheme is shown to be more efficient than the Roe scheme when the S-A one equation turbulence model is coupled.

2.3 The 5th Order WENO Scheme

For reconstruction of the interface flux, $E_{i+\frac{1}{2}} = E(Q_L, Q_R)$, the conservative variables Q_L and Q_R are evaluated by using the 5th order WENO scheme[35, 36]. For example,

$$\left(Q_L\right)_{i+\frac{1}{2}} = \omega_0 q_0 + \omega_1 q_1 + \omega_2 q_2 \tag{48}$$

where

$$q_0 = \frac{1}{3}Q_{i-2} - \frac{7}{6}Q_{i-1} + \frac{11}{6}Q_i \tag{49}$$

$$q_1 = -\frac{1}{6}Q_{i-1} + \frac{5}{6}Q_i + \frac{1}{3}Q_{i+1} \tag{50}$$

$$q_2 = \frac{1}{3}Q_i + \frac{5}{6}Q_{i+1} - \frac{1}{6}Q_{i+2} \tag{51}$$

$$\omega_k = \frac{\alpha_k}{\alpha_0 + \ldots + \alpha_{r-1}} \tag{52}$$

$$\alpha_k = \frac{C_k}{\epsilon + IS_k},\ k = 0, \ldots, r-1 \tag{53}$$

$$C_0 = 0.1,\ C_1 = 0.6,\ C_2 = 0.3 \tag{54}$$

$$IS_0 = \frac{13}{12}\left(Q_{i-2} - 2Q_{i-1} + Q_i\right)^2 + \frac{1}{4}\left(Q_{i-2} - 4Q_{i-1} + 3Q_i\right)^2 \tag{55}$$

$$IS_1 = \frac{13}{12}\left(Q_{i-1} - 2Q_i + Q_{i+1}\right)^2 + \frac{1}{4}\left(Q_{i-1} - Q_{i+1}\right)^2 \tag{56}$$

$$IS_2 = \frac{13}{12}\left(Q_i - 2Q_{i+1} + Q_{i+2}\right)^2 + \frac{1}{4}\left(3Q_i - 4Q_{i+1} + Q_{i+2}\right)^2 \tag{57}$$

ϵ is originally introduced to avoid the denominator becoming zero and is supposed to be a very small number. In the reference[36, 37], it is observed that IS_k will oscillate if ϵ is too small and also shift the weights away from the optimal values in the smooth region. The higher the ϵ values, the closer the weights approach the optimal values, C_k, which will give the symmetric evaluation of the interface flux with minimum numerical dissipation. When there are shocks in the flow field, ϵ can not be too large to maintain the sensitivity to shocks. In reference[36, 37], $\epsilon = 10^{-2}$ is recommended for the transonic flow with shock waves. The viscous terms used 2nd order central differencing scheme.

2.4 Time Marching Scheme

The time dependent governing equation (1) is solved using dual time stepping method suggested by Jameson[38]. A pseudo temporal term $\frac{\partial Q}{\partial \tau}$ is added to the governing Eq. (1). This term vanishes at the end of each physical time step, and has no influence on the accuracy of the solution. An implicit pseudo time marching scheme using Gauss-Seidel line relaxation is employed to achieve high convergence rate instead of using the explicit scheme[37]. The pseudo temporal term is discretized with first order Euler scheme. Let m stand for the iteration index within a physical time step, the semi-discretized governing equation can be expressed as

$$\begin{aligned}\left[\left(\tfrac{1}{\Delta\tau} + \tfrac{1.5}{\Delta t}\right) I - \left(\tfrac{\partial R}{\partial \mathbf{Q}}\right)^{n+1,m}\right] \delta\mathbf{Q}^{\mathbf{n+1,m+1}} \\ = R^{n+1,m} - \tfrac{3\mathbf{Q}^{\mathbf{n+1,m}} - 4\mathbf{Q}^{\mathbf{n}} + \mathbf{Q}^{\mathbf{n-1}}}{2\Delta t}\end{aligned} \tag{58}$$

where $\Delta\tau$ is the pseudo time step, and R is the net flux of the Navier-Stokes equations.

3 Structural Model

3.1 Modal Approach

The equation of motion of an N-DOF(degree of freedom) system with mechanical damping and the aerodynamic loading as the excitation force can be presented in matrix form:

$$[\mathbf{M}]\{\ddot{\mathbf{X}}\} + [\mathbf{C}]\{\dot{\mathbf{X}}\} + [\mathbf{K}]\{\mathbf{X}\} = \{\mathbf{F}\} \tag{59}$$

where, **M**, **C**, **K** are the mass, structural damping and stiffness matrices. **F** is total aerodynamic force acting on the wing surface. Total aerodynamic force can be defined as follows:

$$\mathbf{F} = -\oint P \cdot \hat{n} dA + \oint \tau_{\mathbf{w}} \cdot \hat{t} dA \tag{60}$$

where, $\hat{n}$ is the unit normal vector to the wing surface and $\hat{t}$ is the unit tangent vector to the wing surface. P is the fluid static pressure and $\tau_{\mathbf{w}}$ is the fluid wall shear stress acting on the wing surface. Eq. (27) is used to compute static pressure of the wing surface by setting flow velocity components to zero.

To decouple the equations of motion for the damped systems(59), we use the mass normalized mode shape($\tilde{\phi}$) defined as the normal modes divided by square root of the generalized mass($\sqrt{\phi^T m \phi}$). Let $\{\mathbf{X}\} = [\tilde{\Phi}]\{\mathbf{q}\}$ and premultiply Eq. (59) by the transpose $[\tilde{\Phi}]^T$.

$$\begin{aligned}[\tilde{\Phi}]^T[\mathbf{M}][\tilde{\Phi}]\{\ddot{\mathbf{q}}\} + [\tilde{\Phi}]^T[\mathbf{C}][\tilde{\Phi}]\{\dot{\mathbf{q}}\} + [\tilde{\Phi}]^T[\mathbf{K}][\tilde{\Phi}]\{\mathbf{q}\} \\ = [\tilde{\Phi}]^T\{\mathbf{F}\}\end{aligned} \tag{61}$$

where **q** is the vector of the principal coordinates. Using the orthogonality of the system matrices and assuming damping matrix to be a linear combination of the mass and stiffness matrices, Eq. (61) is then completely decoupled and the jth equation will have the form

$$\ddot{q}_j + 2\zeta_j\omega_j\dot{q}_j + \omega_j^2 q_j = \frac{\tilde{\phi}_j^T}{m_j}\mathbf{F} \tag{62}$$

where $[\tilde{\Phi}]^T = [\tilde{\phi}_1, \cdots, \tilde{\phi}, \cdots, \tilde{\phi}_N]^T$. N is the number of modal coordinates. ω_j and ζ_j are natural frequency and modal damping ratio for mode j. m_j denotes the jth diagonal element of modal mass matrix that is unity. In the current study, the structural system is reduced to only five mode shapes. The normalized modal equation can be given as[39]

$$\ddot{q}_j + 2\zeta_j(\tfrac{\omega_j}{\omega_\alpha})\dot{q}_j + (\tfrac{\omega_j}{\omega_\alpha})^2 q_j = \frac{\tilde{\phi}_j^{*T}}{m_j^*} \cdot \mathbf{F}^* \cdot {V_f}^2 \cdot \frac{b_s^2 L}{\bar{V}} \cdot \bar{m} \tag{63}$$

where the dimensionless quantities are denoted by an asterisk. $V_f(= \frac{U_\infty}{b_s\omega_\alpha\sqrt{\bar{\mu}}})$ is the flutter speed index which is an input flutter control parameter. $\bar{m}$ is the measure wing panel mass, $\bar{V}$ represents the conical frustum volume and b_s is the streamwise root semi chord. L is the reference length and ω_α is the angular frequency of the first torsional mode in units of $radians/sec$. $\bar{\mu}(= \frac{\bar{m}}{\bar{V}\rho_\infty})$ stands for the mass ratio, i.e. the ratio between the structural mass and the mass of the equivalent volume of fluid at reference density. It is noticed that m_j^* should be equal to one when the mass normalized mode shapes are used. For example, the mode shapes of AGARD wing 445.6 Weakend model 3 reported by Yates[40] are normalized using the generalized mass such that m_j^* equals one in units $lbf \cdot in \cdot s^2$. This corresponds to 0.112979 $kg \cdot m^2$ in SI units.

The structure equations are then transformed to a state form as follows:

$$[\mathbf{M}]\frac{\partial \mathbf{S}}{\partial t} + [\mathbf{K}]\{\mathbf{S}\} = \mathbf{q} \tag{64}$$

where

$$\mathbf{S} = \begin{pmatrix} q_j \\ \dot{q}_j \end{pmatrix}, \mathbf{M} = [I], \mathbf{K} = \begin{pmatrix} 0 & -1 \\ (\frac{\omega_j}{\omega_\alpha})^2 & 2\zeta_j(\frac{\omega_j}{\omega_\alpha}) \end{pmatrix}$$

$$\mathbf{q} = \begin{pmatrix} 0 \\ \phi_j^{*T} \cdot \mathbf{F}^* \cdot V_f \cdot \frac{b_s^2 L}{\bar{V}} \cdot \bar{m} \end{pmatrix}$$

3.2 Implicit Structural Solver

To solve the structural equations with CFD solver[30, 31] in a fully coupled manner[39], the decoupled structural equations are integrated using the same method as the flow governing equations(58) within each physical time step:

$$\begin{gathered} \left(\frac{1}{\Delta\tau}I + \frac{1.5}{\Delta t}M + K\right)\delta S^{n+1,m+1} \\ = q^{n+1,m+1} - M\frac{3S^{n+1,m} - 4S^n + S^{n-1}}{2\Delta t} - KS^{n+1,m} \end{gathered} \tag{65}$$

Within each physical time step, the flow equations and structural equations are solved iteratively via every successive pseudo time step until the prescribed convergence criteria is satisfied for both flow and structural solver. After the convergence criteria is reached, the fluid-structural interaction goes to next physical time step.

4 Computational Model

The configuration simulated is tested at AFRL Aerospace Systems Directorate large-scale RC-19 supersonic combustion research cell[41], as shown in Fig. 1. The position of shock generator is carefully controlled so that the oblique shock hits the vibrating panel on the top side of the test section. The detailed geometry parameters can be found in the paper of Gogulapati et al[11]. The compliant panel has dimensions L = 254 mm, S= 127 mm, and h = 0.635 mm. The wedge angle of the shock generator is 8°. It should be noted that the cross section of the shock generator is not a isosceles triangle.

The computational mesh for the shock generator model is shown in Fig. 2. A mesh topology that aligns with shock angle is created to capture the oblique shock wave and its reflection on the panel. The incline angle of mesh is determined by shock angle based on the wedge angle and the incoming Mach number. For comparison, a mesh distributed in the streamwise direction normal to the axis is also shown in Fig. 2. The total number of grid points is 6939297 with 417 points in streamwise direction, 129 points in the transverse direction and 129 points in the spanwise direction. The mesh is clustered near the wall to resolve the turbulent boundary layer. Total 264 CPUs are used for the simulation with parallel computing.

The inlet boundary conditions[11] for the computational domain is total pressure p_0 = 345kPa, total temperature T_0 = 290K, and M=2.0. All other variables are fixed based on these conditions for supersonic inlet flow, zero gradient BC for the outlet, no slip and isothermal BC for top and bottom wall. The slip BCs for side walls are used as shown in Fig. 3 to save CPU cost to avoid resolving side wall boundary layers, which are considered as having secondary effect on the panel aeroelasticity caused by STBLI. In the experiment, a pressure ports was added to the top section of the tunnel wall

downstream of the panel in order to prevent panel failure during tunnel start-up. This study uses the static pressure right downstream of the panel to mimic the tunnel test during FSI simulation.

The non-dimensional physical time step used in the simulation is 0.05. The CFL number used for the pseudo time step is 1. Typically, it takes 30 iterations to reduce the residual by three orders of magnitude within each physical time step. It takes one week wall clock time to run 0.1s physical time with 264 CPUs using parallel computing. Since it is a fully coupled fluid-structural interaction simulation, the flow and structure response are captured by the solver itself with no parameter adjustment.

5 Results and discussion

An initial investigation of the flow is undertaken aiming to identify the effect of length of inlet duct and the side walls and assess the capability of DDES computations for this flow case. A steady state RANS simulation was firstly conducted to examine if the shock waves positions are captured correctly. With a 8° wedge, shock angle is about 39° at free stream M=2.0. To achieve the correct boundary layer thickness that creates a shock angle of 39°, the inlet length is iterated until the shock impingement position matches the one measured in the experiment. Fig. 4 shows the Mach number contour from the final computational domain that generates satisfactory shock angle and impingement position.

The effect of the incline mesh topology is evaluated by comparing with a vertical mesh. Fig. 5 shows the Mach contours of the vertical mesh. The shock angle of the first oblique shock agree very well with that captured by the inclined mesh as shown in Fig. 4. So is the shock reflection. However, the triple point phenomenon in vertical mesh is captured more clearly than that in the inclined mesh model. The inclined mesh shows overall higher resolution of the front shock and its reflection than that in the vertical mesh model. Because it is more convenient to implement the FSI simulation with a vertical mesh, the unsteady and FSI simulation employ the vertical mesh in this study. Mesh refinement study is conducted by using a total 63 million grid points in the refined mesh. Even though the shock wave and expansion wave of refined mesh are captured with higher resolution as show in the right plot of Fig. 5, the magnitude of the pressures are very similar between the coarse and refined mesh. Due to high CPU cost of the refined mesh, the panel FSI simulation uses the coarse mesh.

The first five mode shapes of the panel are obtained by using ABAQUS software and are shown in Fig. 6. The natural frequencies of the first 5 modes are f1=236 Hz, f2=306 Hz, f3=433 Hz, f4=612 Hz, f5=618 Hz. The computed results are in excellent agreement with that from Gogulapati[11].

Fig. 7 shows modal displacement of the first five modes of the panel. A dynamically stable vibration is achieved after the physical time of about 0.6s. The vibration is similar to a limited cycle oscillation as shown in Fig. 8. The first mode has the largest contribution to the physical displacement amplitude among the first five modes. The contributions of the second and the third modes are almost the same and are substantially smaller than that of the first mode as shown in Fig. 7. The contributions of the fourth and fifth mode are almost negligible compared to that of the first mode.

Fig. 8 illustrates physical displacements in center-line of the panel. The largest displacement occurs near the center point of the panel instead of the shock impingement point. The corresponding spectrum analysis of physical displacement are shown in Fig. 9. The maximum predicted mean displacement during the vibration is about 0.19 mm. The predicted displacement is close to that measured in the experiment[41], which is 0.089 mm. In the simulation of Gogulapati, et al.[11], the computed mean displacements for the unheated cases is 0.886 mm, which is substantially more over predicted than the present results. The dominant frequency predicted by the present FSI simulation is the 236 Hz, which is very close to the measured frequency and is the same as the natural frequency of the first mode.

Fig. 10 is Mach contours at three spanwise locations. Since the slip boundary conditions are used on the side walls to reduce CPU cost, the Mach number contours are similar along the span. Fig.

11 displays pressure contours at three spanwise locations. Fig. 12 shows pressure contours at three horizontal surfaces, bottom wall, middle plane and upper wall. It is clearly seen that there are high pressure jumps at shock generator location, mid-channel shock and its reflections impingement locations. The time history of pressure along the center line of the panel is shown in Fig. 13. It is seen that there is a large pressure fluctuation during the panel vibration.

6 Conclusions

In this paper, delayed detached eddy simulation is performed to simulate a supersonic panel vibration at Mach 2.0. Unsteady 3D compressible Navier-Stokes equations are solved with a system of 5 decoupled structure modal equations in a fully coupled manner. The low diffusion E-CUSP scheme with a 5th order WENO reconstruction for the inviscid flux and a set of 2nd order central differencing for the viscous terms are used to accurately capture the shock wave/turbulent boundary layer interaction of the vibrating panel.

The shock waves and their reflection interacting with turbulent boundary layer in the tunnel are well captured by the DDES. The panel vibration induced by the shock boundary layer interaction is well resolved. The dominant panel response agrees with the experiment in terms of the mean panel displacement and frequency. Even though the linear model structure model performs very well in this simulation, the next step would be to incorporate nonlinear finite element model to further improve the accuracy. It takes one week wall clock time to run 0.1s physical time with 264 CPUs using parallel computing. Since it is a fully coupled fluid-structural interaction simulation, the flow and structure responses are captured by the solver itself with no parameter adjustment.

7 Acknowledgment

The computing resource support from the Center for Computational Sciences at University of Miami and the High Performance Computing Challenge Project of DoD Supercomputing Resource Centers are greatly appreciated.

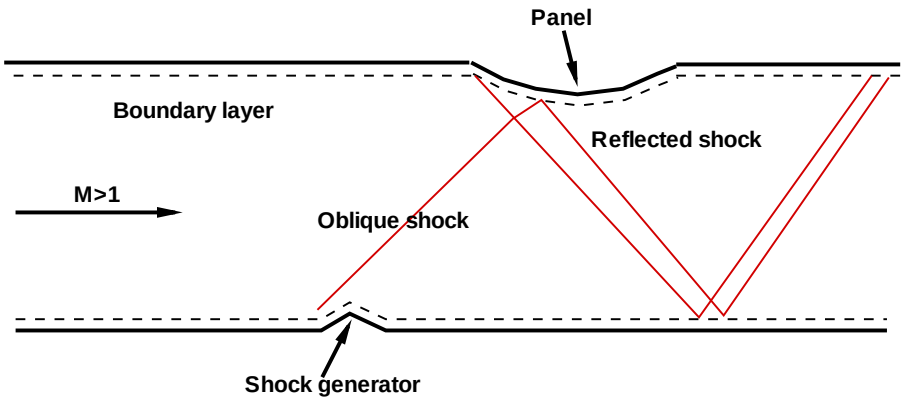

Figure 1: Computational configuration of shock wave turbulent boundary layer interaction

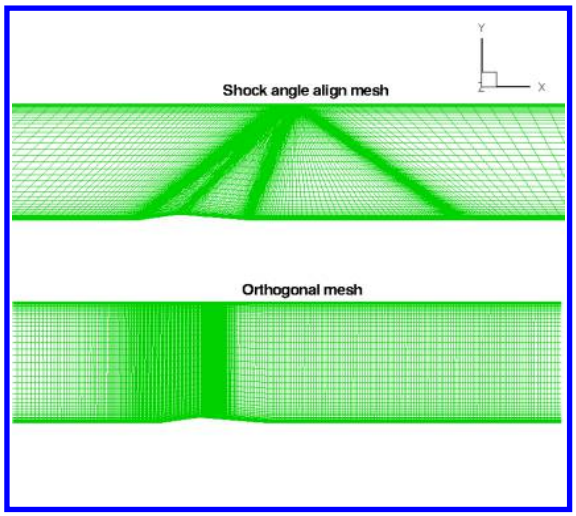

Figure 2: Different computational mesh

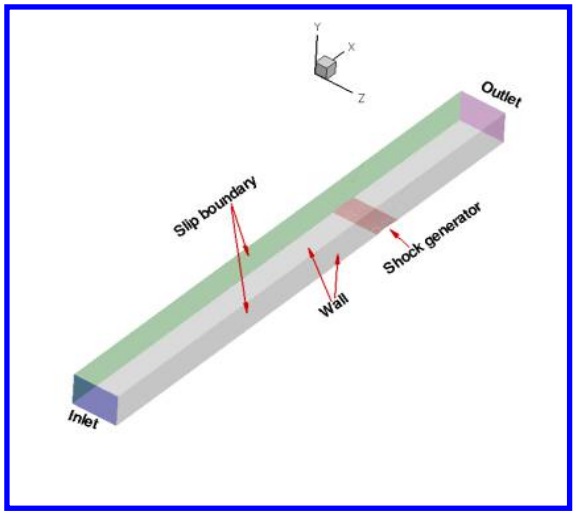

Figure 3: Boundary condition of the domain

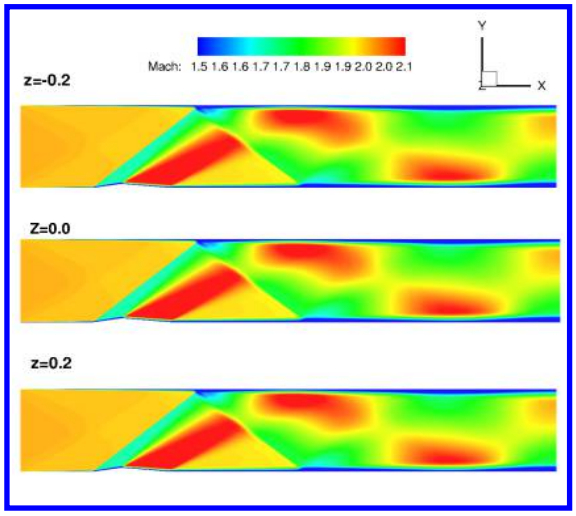

Figure 4: Mach number contours of the inclined mesh

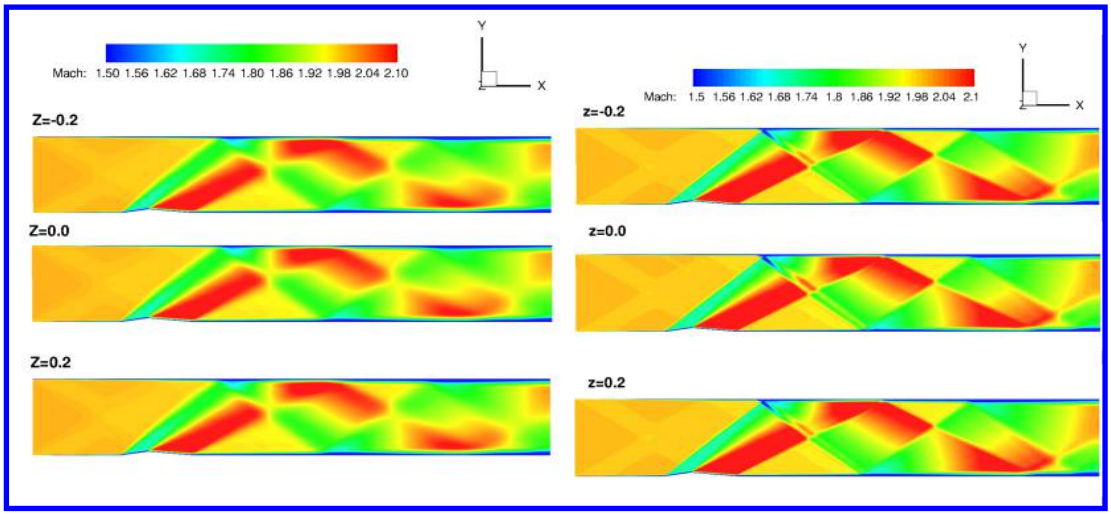

Figure 5: Mach number contours of the vertical mesh, coarse mesh(left), refined mesh(right)

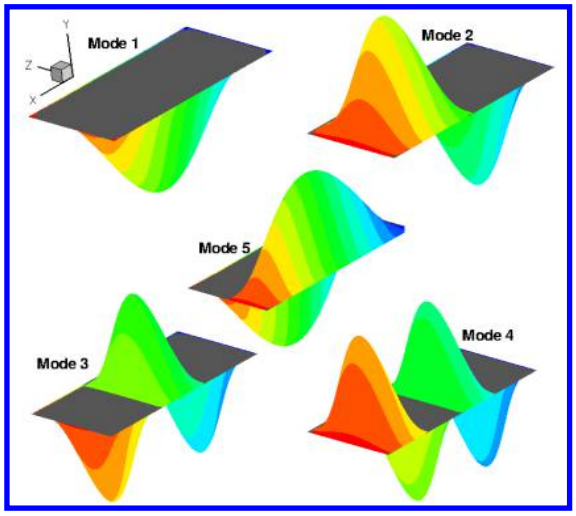

Figure 6: The first 5 mode shapes of the steel panel

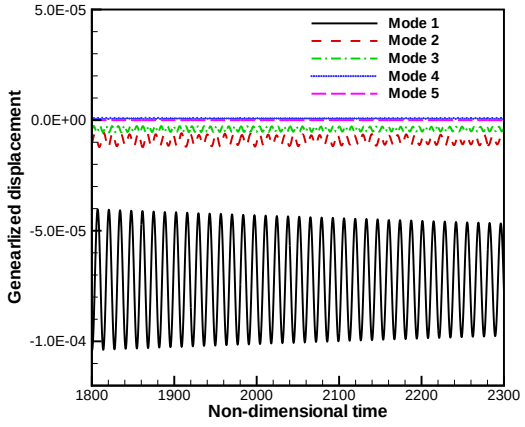

Figure 7: Time history of modal displacement.

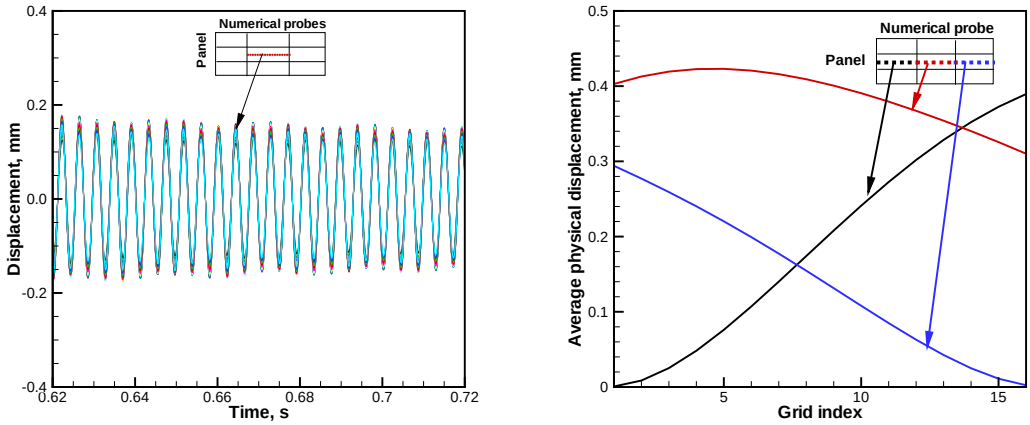

Figure 8: Time history(left) and time average(right) of physical displacement in the center of panel.

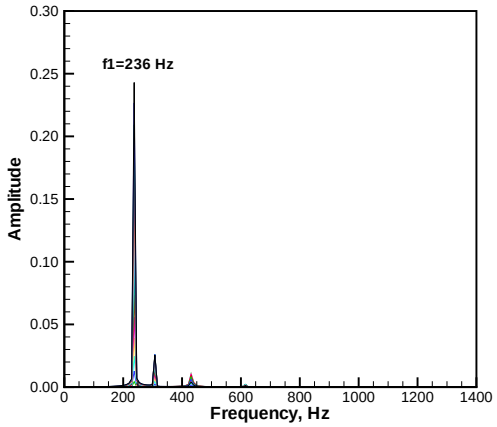

Figure 9: Spectrum of physical displacement in the center-line of panel.

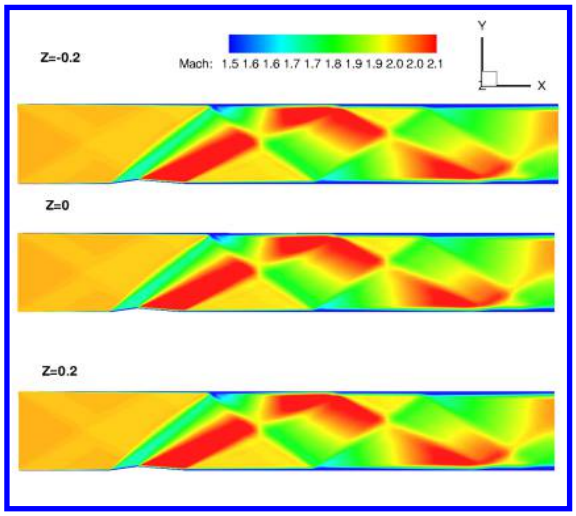

Figure 10: Mach contour showing the shock wave during panel vibration.

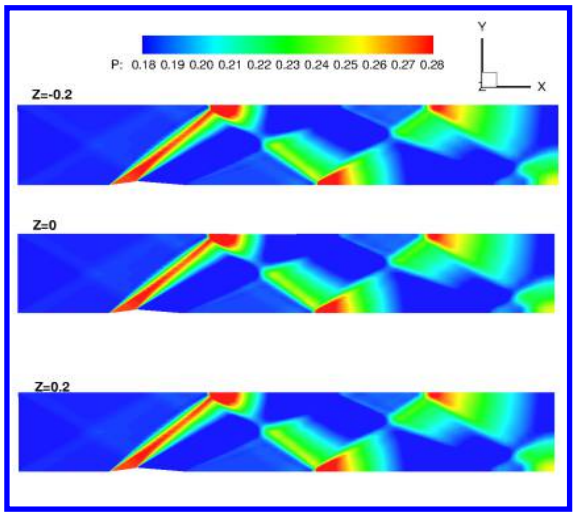

Figure 11: Pressure contour in spanwise sections.

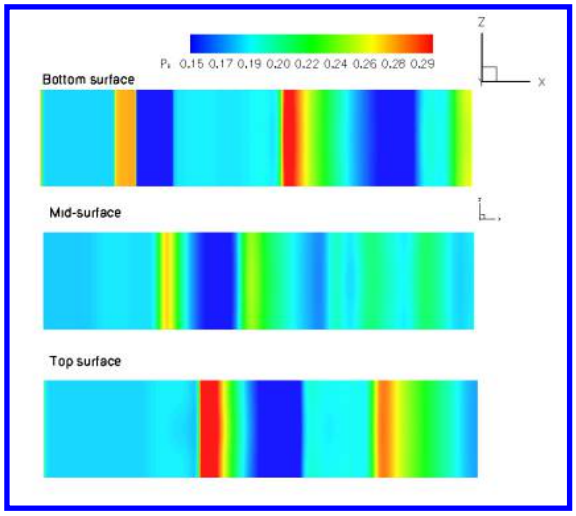

Figure 12: Pressure contour in horizontal sections.

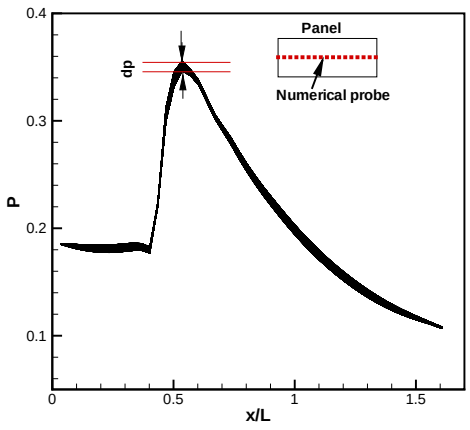

Figure 13: Time history of pressure along center line of the panel with the width of the line representing the range of pressure

References

[1] Dowell, E.H., "Panel flutter: a review of the aeroelastic stability of plate and shells.," *AIAA Journal*, vol. 8, pp. 385–399, 1970.

[2] Mei C, Abdel-Motagaly K, Chen R., "Review of nonlinear panel flutter at supersonic and hypersonic speeds," *Applied Mechanics Reviews*, vol. 52, pp. 321–332, 1999.

[3] S. Priebe, M. Martin, "Direct Numerical Simulation of Shockwave and Turbulent Boundary Layer Interactions." AIAA-2009-0589, 47th AIAA Aerospace Sciences Meeting, January 5-8, Orlando, FL, USA, 2009.

[4] Knight, D., Yan, H., Panaras, A. G., Zheltovodov, A., "Advances in CFD Prediction of Shock Wave Turbulent Boundary Layer Interactions," *Progress in Aerospace Sciences*, vol. 39, pp. 121–184, 2003.

[5] Sinha, K., Mahesh, K., Candler, G., "Modeling the Effect of Shock Unsteadiness in Shock/Turbulent Boundary-Layer Interactions," *AIAA Journal*, vol. 43, pp. 586–594, 2005.

[6] Morgan, B., Kawai, S., Lele, S. K., "Large-Eddy Simulation of an Oblique Shock Impinging on a Turbulent Boundary Layer." AIAA Paper 2010-4467, 40th Fluid Dynamics Conference and Exhibit, June 28 - July 1, Chicago, Illinois, 2010.

[7] P.R. Spalart, S. Deck, M. Shur, and K.D. Squires, "A New Version of Detached-Eddy Simulation, Resistant to Ambiguous Grid Densities," *Theoritical and Computational Fluid Dynamics*, vol. 20, pp. 181–195, 2006.

[8] F.R. Menter, and M. Kuntz, "Adaptation of Eddy-Viscosity Turbulence Models to Unsteady Separated Flow Behind Vehilces, *The Aerodynamics of Heavy Vehicles: Trucks, Buses and Trains, Edited by McCallen, R. Browand, F. and Ross, J.* ," *Springer, Berlin Heidelberg New York, 2004*, 2-6 Dec. 2002.

[9] Crowell, A. R., Miller, B. A., and McNamara, J. J., "Computational Modeling for Conjugate Heat transfer of Shock-SurfaceInteractions on Compliant Skin Panels." 13th AIAA Dynamics Specialists Conference, Denver, CO, April 4-7 2011, pp.1-18, AIAA Paper 2011-2017., 2011.

[10] Dechaumphai, P., Wieting, A., Thornton, E., "Flow-thermal-structural study of aerodynamically heated leading edges," *Journal of Spacecraft and Rockets*, vol. 26, pp. 201–209, 1989.

[11] A. Gogulapati , R. Deshmukh y, A. R. Crowell y, and J. J. McNamara, "Response of a Panel to Shock Impingement: Modeling and Comparison with Experiments." AIAA 2014-0148, 55th AIAA/ASMe/ASCE/AHS/SC Structures, Structural Dynamics, and Materials Conference, 13-17 January 2014, National Harbor, Maryland, 2014.

[12] R. B. Melville, S. A. Morton, and D. P. Rizzetta, "Implementation of a Fully-Implicit, Aeroelastic Navier-Stokes Solver." AIAA Paper-97-2039, 1997.

[13] E. M. Lee-Rausch, and J.T. Batina, "Calculation of AGARD wing 445.6 flutter using Navier-Stokes aerodynamics." AIAA Paper 1993-3476, August 9-11, 1993.

[14] R. B. Melville and S. A. Morton, "Fully Implicit Aeroelasticity on Oveerset Grid Systems ." AIAA Paper-98-0521, 1998.

[15] S. A. Morton, R. B. Melville, and M. R. Visbal, "Accuracy and Coupling Issues of Aeroelastic Navier-Stokes Solutions on Deforming Meshes." AIAA Paper-97-1085, 1997.

[16] R. Gordnier and M. R.B., "Transonic Flutter Simulations Using an Implicit Aeroelastic Solver," *Journal of Aircraft*, vol. 37, pp. 872–879, September-October 2000.

[17] F. Liu, Y. Zhu, H. Tsai, and A. Wong, "Calculation of Wing Flutter by a Coupled Fluid-Structure Method," *Journal of Aircraft*, vol. 38, pp. 334–342, 2001.

[18] Shen, Y.-Q. and Zha, G.-C. and Chen, X.-Y., " High Order Conservative Differencing for Viscous Terms and the Application to Vortex-Induced Vibration Flows," *Journal of Computational Physics*, vol. 228(2), pp. 8283–8300, 2009.

[19] Shen, Y.-Q. and Zha, G.-C. and Chen, X.-Y., " High Order Conservative Differencing for Viscous Terms and the Application to Vortex-Induced Vibration Flows," *Journal of Computational Physics*, vol. 228(2), pp. 8283–8300, 2009.

[20] Wang, B. Y and Zha, G.-C., "High Fidelity Simulation of Nonlinear Fluid-Structural Interaction with Transonic Airfoil Limit Cycle Oscillations," *Journal of Fluids and Structures*, vol. doi:10.1016/j.jfluidstructs.2010.02.003, 2010.

[21] Wang, B. Y and Zha, G.-C., "Detached-Eddy Simulation of Transonic Limit Cycle Oscillations Using High Order Schemes," *Journal of Computer & Fluids*, vol. 52, pp. 58–68, 2011.

[22] Im, H-S., Chen, X-Y and Zha, G-C., " Detached Eddy Simulation of Rotating Stall Inception for a Full Annulus Transonic Rotor ," *AIAA Journal of Propulsion and Power*, vol. 28, No. 4, pp. 782–798, 2012.

[23] X.Y. Chen, G.-C. Zha, M.-T. Yang, "Numerical Simulation of 3-D Wing Flutter with Fully Coupled Fluid-Structural Interaction," *Journal of Computers & Fluids*, vol. 36, pp. 856–867, 2007, doi:10.1016/j.compfluid.2006.08.005.

[24] H.-S. Im, and G.-C. Zha, "Flutter Prediction of a Transonic Fan with Traveling Wave Using Fully Coupled Fluid/Structure Interaction." ASME Paper GT2013-94341, Proceedings of ASME Turbo Expo, San Antonio, Texas, USA, 2013.

[25] Im, H.-S. and Zha, G.-C., "Prediction of a Supersonic Wing Flutter Boundary Using a High Fidelity Detached Eddy Simulation." AIAA Paper 2012-0039, 50th AIAA Aerospace Sciences Meeting, Jan. 9-12., Nashville, TN, USA, 2012.

[26] Gan, J.Y., Im, H.S., Chen, X.Y., Pasiliao, C.L. and Zha, G.C., "Prediction of Wing Flutter Boundary Using High Fidelity Delayed Detached Eddy Simulation." AIAA Paper 2015, Kissimmee, Florida, Jan. 2015.

[27] X.Y. Chen, and G.-C. Zha, "Fully Coupled Fluid-Structural Interactions Using an Efficient High Solution Upwind Scheme," *Journal of Fluid and Structure*, vol. 20, pp. 1105–1125, 2005.

[28] P.R. Spalart, and S.R. Allmaras, "A One-equation Turbulence Model for Aerodynamic Flows." AIAA-92-0439, 1992.

[29] M. Shur, P.R. Spalart, M. Strelets, and A. Travin, "Detached-Eddy Simulation of an Airfoil at High Angle of Attack", 4th Int. Symp. Eng. Turb. Modelling and Measurements, Corsica." May 24-26, 1999.

[30] G.C. Zha, Y.Q. Shen, and B.Y. Wang, "An improved low diffusion E-CUSP upwind scheme ," *Journal of Computer and Fluids*, to appear 2011.

[31] G.C. Zha, Y.Q. Shen, and B.Y. Wang, "Calculation of Transonic Flows Using WENO Method with a Low Diffusion E-CUSP Upwind Scheme." AIAA Paper 2008-0745, 46th AIAA Aerospace Sciences Meeting, Reno, NV, Jan. 2008.

[32] P. Roe, "Approximate Riemann Solvers, Parameter Vectors, and Difference Schemes," *Journal of Computational Physics*, vol. 43, pp. 357–372, 1981.

[33] J. Edwards, "A Low-Diffusion Flux-Splitting Scheme for Navier-Stokes Calculations," *Computer & Fluids*, vol. 6, pp. 635–659, 1997.

[34] B.Y. Wang, and G.C. Zha, "Comparison of a Low Diffusion E-CUSP and the Roe Scheme for RANS Calculation." AIAA Paper 2008-0596, 46th AIAA Aerospace Sciences Meeting and Exhibit, Jan. 7-10, 2008.

[35] Shen, Y.Q., and Zha, G.C., "Improvement of the WENO Scheme Smoothness Estimator," *International Journal for Numerical Methods in Fluids*, vol. 64,, pp. 653–675, DOI:10.1002/fld.2186, 2009.

[36] Shen, Y.Q., Zha, G.C., and Wang, B.Y., "Improvement of Stability and Accuracy of Implicit WENO Scheme," *AIAA Journal*, vol. 47, pp. 331–334, DOI:10.2514/1.37697, 2009.

[37] Y.Q. Shen, B.Y. Wang, and G.C. Zha, "Implicit WENO Scheme and High Order Viscous Formulas for Compressible Flows ." AIAA Paper 2007-4431, 2007.

[38] A. Jameson, "Time Dependent Calculations Using Multigrid with Applications to Unsteady Flows Past Airfoils and Wings." AIAA Paper 91-1596, 1991.

[39] X.Y. Chen, G.-C. Zha, M.-T. Yang, "Numerical Simulation of 3-D Wing Flutter with Fully Coupled Fluid-Structural Interaction," *Journal of Computers & Fluids*, vol. 36, pp. 856–867, 2007.

[40] E.C. Yates Jr., "AGARD standard aeroelastic configurations for dynamic response. Candidate configuration I.-wing 445.6 ." NASA-TM-1000492, 1987.

[41] Spottswood, S. M., Beberniss, T., and Eason, T., "Full-Field Dynamic Pressure and Displacement Measurements of a Panel Excited by Shock Boundary-Layer Interaction." AIAA Paper 2013-2016, May, 2013.